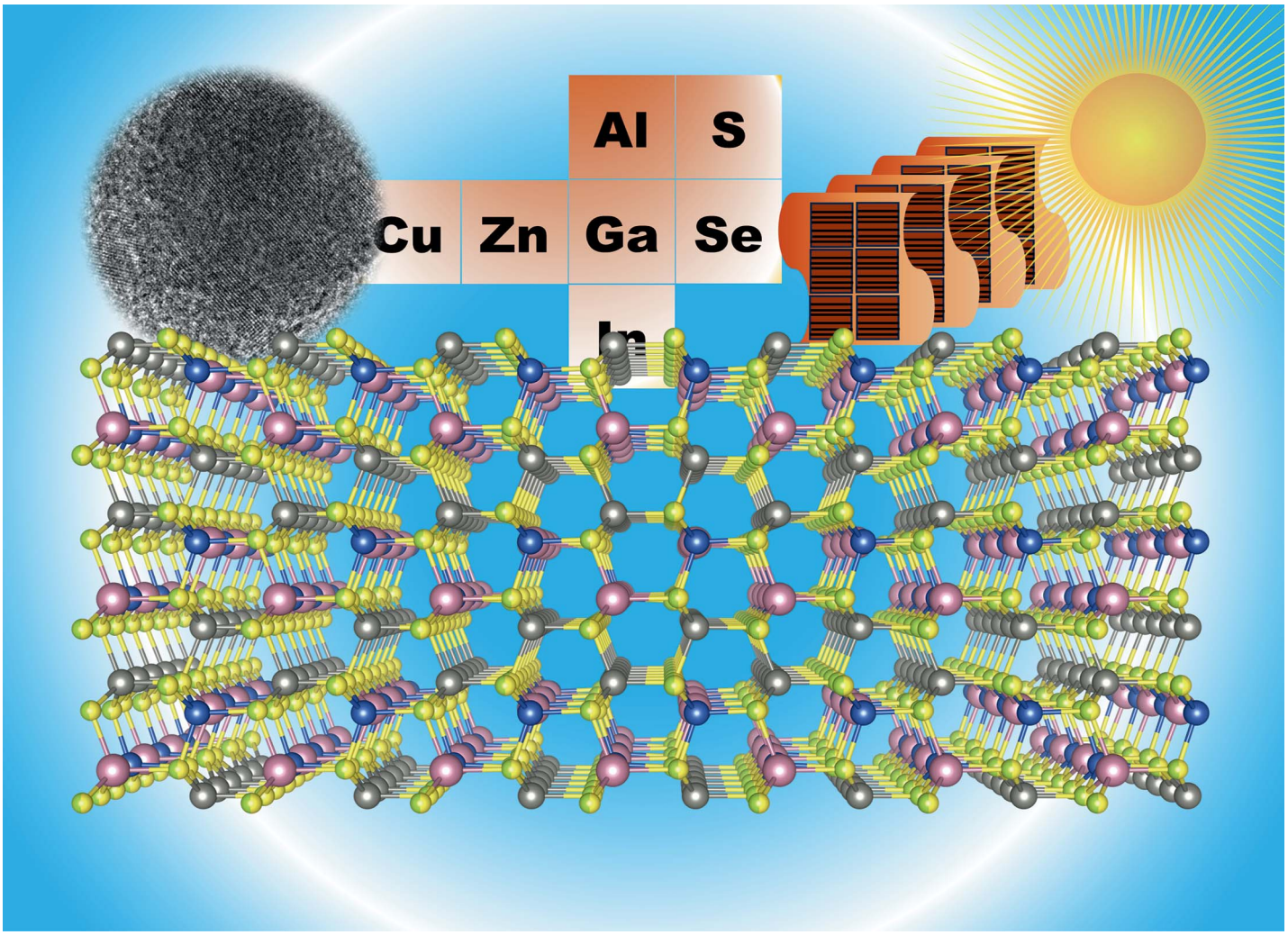

Showcasing research from Dr. Soubantika Palchoudhury's laboratory, Chemical and Materials Engineering, University of Dayton, Ohio 45460, USA.

Multinary light absorbing semiconductor nanocrystals with diversified electronic and optical properties

This work highlights the major breakthrough in research at the rich interface of nanochemistry and theoretical electronic structure prediction for a family of new multinary chalcogenide semiconductor nanocrystals, $CuZn_2AS_xSe_{4-x}$ (A: Al, In, Ga; $0 < x < 4$). A fundamental understanding of tunable electronic properties of the Cu-chalcogenide nanocrystals is achieved *via* synthesis and multi-modal material characterization coupled with density functional theory and virtual crystal approximation. This work showcases the progress of sustainable chalcogenide nanostructures for photovoltaic and light-emitting applications.

As featured in:

See Soubantika Palchoudhury, Jingsong Huang *et al.*, *Nanoscale Adv.*, 2024, **6**, 3785.

ROYAL SOCIETY OF CHEMISTRY

rsc.li/nanoscale-advances

Registered charity number: 207890

Nanoscale Advances

ROYAL SOCIETY OF CHEMISTRY

PAPER

View Article Online
View Journal | View Issue

Cite this: *Nanoscale Adv.*, 2024, **6**, 3785

Multinary light absorbing semiconductor nanocrystals with diversified electronic and optical properties†

Soubantika Palchoudhury, *[a] Benjamin T. Diroll, [b] Panchapakesan Ganesh, [c] Jessica Cobos,[d] Sohini Sengupta[a] and Jingsong Huang *[c]

Received 17th January 2024
Accepted 30th May 2024

DOI: 10.1039/d4na00043a

rsc.li/nanoscale-advances

We report multinary $CuZn_2AS_xSe_{4-x}$ semiconductor nanocrystals in a wurtzite phase, achieved *via* hot-injection synthesis. These nanocrystals exhibit a tunable bandgap and photoluminescence in the visible range. We employ density functional theory and virtual crystal approximation to reveal the bandgap trends influenced by the main group metals and S/Se alloying.

Introduction

There is an increasing demand for sustainable light absorbing as well as light emitting materials, crucial for next-generation clean energy devices and deep tissue bioimaging applications.[1–3] Material choice in thin film solar cells, one of the most attractive solar energy conversion technologies, can greatly impact their performance. Although widely used as the absorber layer, Si is an indirect bandgap material with weak near-infrared (IR) absorption of the solar spectrum, which necessitates the thin film design of solar cells.[4,5] In comparison, Cu-based chalcogenide semiconductor nanocrystals, which exhibit direct bandgap and absorption in the larger visible regime of the solar spectrum, have been explored to maximize the efficiency of thin film solar cells.[6] $Cu(In,Ga)Se_2$ (CIGS) thin film photovoltaics, for instance, have achieved an efficiency of ~23%, the highest so far.[7,8] There has been a continued search for materials composed of earth-abundant elements like Cu_2ZnSnS_4 (CZTS) to achieve desired grid parity, although at the cost of sacrificing the overall efficiency of the solar cell.[9–12] To this end, multinary Cu-chalcogenide compositions have been explored as they offer a higher level of flexibility in terms of tunable bandgap and structure–property relation.[13–16] Similarly, advanced materials play a pivotal role in biomedical imaging. Current research in this field focuses on deep tissue imaging and early-stage cancer detection,[17,18] both of which require tunable light-emitting materials in the IR and visible regimes. However, most of the imaging agents currently used for deep tissue and early cancer diagnostics consist of toxic heavy metals like Hg, Cd, and Pb.[19–21] Recently, Cu-based $CuInSe_xS_{2-x}$/ZnS nanocrystals have shown great promise in bioimaging applications and are more biocompatible as compared to the heavy metal-based imaging agents.[22,23] To this end, multinary Cu-chalcogenide semiconductor nanocrystals can offer a wider range of flexibility in emissive properties. However, these multinary semiconductor nanocrystal compositions are synthetically challenging to achieve.

Herein, we report the colloidal synthesis of a new class of multinary $CuZn_2AS_xSe_{4-x}$ (A: Al, Ga, In; $0 < x < 4$; CZASSe) chalcogenide semiconductor nanocrystals and a combined experimental and theoretical investigation of their composition-dependent optical and emissive properties. The composition, morphology, and crystal structure of the new semiconductor nanocrystals have been explored in detail *via* transmission electron microscopy (TEM), scanning electron microscopy energy dispersive X-ray (SEM-EDX), and X-ray diffraction (XRD), while the optical bandgap and emission properties of the corresponding chalcogenide compositions have been investigated *via* ultraviolet-visible spectroscopy (UV-vis) and photoluminescence (PL). Synergistic *ab initio* density functional theory (DFT) calculations employing both the Strongly Constrained and Appropriately Normed (SCAN) meta-Generalized Gradient Approximation (GGA) and Heyd–Scuseria–Ernzerhof (HSE06) hybrid functionals, in conjunction with the virtual crystal approximation (VCA), are used to elucidate the bandgap trends associated with the main group metals and S/Se alloying.[24–26]

[a]*Department of Chemical and Materials Engineering, University of Dayton, Dayton, Ohio 45469, USA. E-mail: spalchoudhury1@udayton.edu; Tel: +1-937-229-3194*

[b]*Center for Nanoscale Materials, Argonne National Laboratory, Lemont, Illinois 60439, USA*

[c]*Center for Nanophase Materials Sciences, Oak Ridge National Laboratory, Oak Ridge, Tennessee 37831, USA. E-mail: huangj3@ornl.gov; Tel: +1-865-576-3991*

[d]*Department of Aerospace and Mechanical Engineering, University of Texas at El Paso, El Paso, Texas 79968, USA*

† Electronic supplementary information (ESI) available: Experimental details for synthesis and characterization of the CZASSe nanocrystals, details of the computational studies, SEM and EDX analysis of the CZASSe nanocrystals, PL analysis of the $CuZn_2AlSSe$ and $CuZn_2InSSe$ nanocrystals, XRD analysis and Rietveld fit of the CZASSe nanocrystals, experimental bandgap and a table summarizing the bandgaps of CZASSe nanocrystals, and band structure and density of states of the $CuZn_2AlSSe$ and $CuZn_2InSSe$ nanocrystals. See DOI: https://doi.org/10.1039/d4na00043a

Experimental and theoretical methods

We report in this section the synthesis and characterization of $CuZn_2AS_xSe_{4-x}$ (CZASSe, A: Al, Ga, In, $0 < x < 4$) nanocrystals and the computational studies of the electronic properties using density functional theory.

Materials. Chemicals used in this project were purchased from Sigma-Aldrich, Thermo Scientific, Strem Chemicals, Alfa Aesar, TCI, VWR, and Fisher. They were used as purchased without any modification. These include: copper(II) acetylacetonate ($Cu(acac)_2$, ACROS, 98%), zinc(II) acetylacetonate ($Zn(acac)_2$, Thermo Scientific), deionized water (DI, VWR), indium(III) acetylacetonate ($In(acac)_3$, Alfa Aesar, 98%), gallium(III) acetylacetonate ($Ga(acac)_3$, Strem Chemicals, 99.99%), aluminum(III) acetylacetonate ($Al(acac)_3$, Thermo Scientific, 97%), oleylamine (OLA, Sigma Aldrich, 70%), 1-dodecanethiol (*n*-DDT, ACROS, 98%), *tert*-dodecanethiol (*t*-DDT, TCI), diphenyl diselenide (Sigma Aldrich, 98%), hexane (Fisher), and ethanol (Fisher).

Synthesis of CZASSe nanocrystals. The CZASSe nanocrystals were synthesized *via* a modified hot-injection route under an inert nitrogen atmosphere using a Schlenk line technique.[13] In a typical synthesis of a representative CZASSe composition, $CuZn_2InS_2Se_2$, stoichiometric quantities of the cationic precursors *i.e.*, $Cu(acac)_2$ (0.1 mmol), $Zn(acac)_2$ (0.2 mmol), and $In(acac)_3$ (0.1 mmol) were stirred in 10 mL of the OLA for 30 min under a nitrogen purge. The OLA served as the solvent, reducing agent, as well as the ligand in the reaction. The reaction mixture was then heated to 150 °C (heating rate: 16 °C min^{-1}). The chalcogen precursors *i.e.*, a mixture of diphenyl diselenide (0.2 mmol) in *n*-DDT (0.125 mL) and *t*-DDT (0.875 mL) were quickly injected into the reaction mixture at 150 °C as the S and Se sources, prior to heating the reaction at 250 °C for one hour to form the multinary $CuZn_2InS_2Se_2$ nanocrystals. The nanocrystal solution was cooled and cleaned *via* multiple washes in ethanol/hexane solvent mixture using a microcentrifuge (room temperature, 15 000 rpm, 30 min, Sorval™ Legend™ Micro 17 microcentrifuge, Fisher) for further characterization.

All the other compositions of CZASSe nanocrystals were synthesized using a similar process with stoichiometric quantities of the respective cationic and chalcogen precursors, keeping all other conditions the same. The reaction mixtures were heated to 300 °C for the CZAlSSe and CZGaSSe semiconductor nanocrystals.

Characterizations. Well-dispersed solutions of the CZASSe nanocrystals in hexane (concentration $\sim$ 1.5 g L^{-1}) were prepared *via* 30 min sonication at room temperature (Branson 1800, Fisher) to form the samples for photoluminescence (PL) and absorbance studies. The PL characterization was conducted on a Fluoromax spectrofluorometer (Horiba Scientific). The emission spectra of the nanocrystals were measured in the visible 360–1100 nm range at increments of 0.5 nm for a 350 nm excitation source. Time-resolved photoluminescence (TRPL) of the nanocrystals was measured at room temperature with a weak 475 nm pulsed laser source and collected through a spectrometer (Edinburg FLS1000) at a photon multiplier tube. The absorbance spectra were measured on an Agilent Cary 60 ultraviolet-visible spectroscope (UV-vis) and the optical transitions and experimental bandgap of the nanocrystals were estimated from the Tauc plot analysis. Scanning electron microscopy (SEM) analysis was carried out using a Phenom ProX Desktop Generation 5 SEM equipped with energy dispersive X-ray spectroscope (EDX) to investigate the size and morphology of the nanocrystals. The elemental compositions of CZASSe nanocrystals were determined using the SEM-EDX by taking an average of five different scans. Well-dried powder samples for the SEM and EDX were prepared by cleaning the semiconductor nanocrystals through multiple washes in ethanol/hexane mixture *via* centrifugation to remove the remnant organics followed by drying overnight in a vacuum desiccator. A 15 kV electron beam was used for SEM imaging and EDX mapping of the CZASSe nanocrystals. Transmission electron microscopy (TEM) and high-resolution TEM (HRTEM) analyses were performed using a JEOL 2100F TEM with a 200 kV operating beam. Aliquots of well-mixed CZASSe samples in hexane that were prepared *via* a similar process as mentioned for the UV-vis and PL were dropped on 300 mesh copper TEM grids and air dried to prepare the samples for TEM imaging. The crystallographic analyses of the CZASSe nanocrystals were performed by X-ray diffraction (XRD) using a Rigaku SmartLab diffractometer with a Cu Kα ($\lambda = 1.54$ Å) source. Powder samples for XRD were prepared *via* a similar process as used for the SEM sample preparation. XRD measurements were conducted in the 2θ range of 20–70°. Rietveld refinement of the experimental XRD structures of CZASSe nanocrystals were conducted using a GSA-II software (Argonne National Laboratory).

Computational studies. First-principles calculations were done using the Vienna *ab initio* simulation package.[27,28] Kohn–Sham equations were solved by using a projected-augmented wave (PAW) method.[29,30] Structural relaxations for both lattice vectors and atomic positions adopting bulk compositions were done employing the Strongly Constrained and Appropriately Normed (SCAN) meta-Generalized Gradient Approximation (GGA) functional,[24] in conjunction with the virtual crystal approximation (VCA).[26] The relaxed structures were then used for electronic structure calculations employing both the SCAN meta-GGA and Heyd–Scuseria–Ernzerhof (HSE06) hybrid functionals.[25] The kinetic energy cutoff for plane waves was set to 550 eV and the Brillouin-zone integrations were performed on Γ-centered $6 \times 6 \times 6$ *k*-point grid. The convergence criteria for the structural relaxations and electronic self-consistency were respectively set to a Hellmann–Feynman force of 10^{-2} eV $Å^{-1}$ and energy difference of 10^{-6} eV, and the "accurate" precision setting was adopted to avoid wrap around errors. Band structures were sampled along the path specified in ref. 31.

Results and discussion

The novel CZASSe semiconductor nanocrystals have been synthesized *via* a modified hot-injection approach where the respective metal acetylacetonate salts serve as the multiple cationic precursors while a mixture of *n*-dodecanethiol (*n*-DDT)/*tert*-dodecanethiol (*tert*-DDT) and diphenyl diselenide serve as

precursors for the multiple chalcogen anions. This is the first report of the synthesis of multinary Cu-chalcogenide nanocrystals of composition $CuZn_2AS_xSe_{4-x}$ containing both the S and Se chalcogens. Additionally, a comprehensive series of the CZASSe nanocrystals has been achieved in this study for the first time, where the substitution of S with Se has been varied from 0 to 100% (*i.e.*, 0, 25, 50, 75, and 100%) and these five different S/Se substitutions have been realized for three different group III cations (*i.e.*, Al, Ga, and In). It is not trivial to achieve multinary nanocrystals containing different cations and chalcogen anions within the same lattice. Therefore, the study provides a key achievement from the perspective of nanochemical synthesis. Fig. 1a shows the TEM image of a sample CZASSe composition, $CuZn_2InS_2Se_2$ nanocrystals, which exhibit a plate-like morphology of ~9 × 6 × 2 nm dimensions. The high crystallinity of the nanocrystal is evident from the regular lattice fringes in the high-resolution TEM (HRTEM) image (Fig. 1b). The lattice spacing of 0.24 nm correspond to (102) crystal plane of the wurtzite phase. The chemical composition of the nanocrystals based on the SEM-EDX analysis, $Cu_{1.0}Zn_{2.0}In_{0.8}S_{0.7}Se_{1.1}$, is close to the stoichiometric composition in terms of the Cu : Zn : In and S : Se ratios, although it is deficient in anion composition (Fig. 1c). The deviations from stoichiometries suggest possible defects present on the surface of the nanocrystals. The core compositions for all synthesized nanocrystals can be identified to be stoichiometric $CuZn_2AS_xSe_{4-x}$ based on subsequent XRD measurements and DFT calculations.

The $CuZn_2InS_2Se_2$ nanocrystals also exhibit PL emissions in the blue (467 nm) and green (557 nm) visible ranges with an excitation at 350 nm (Fig. 1d). The emission in the blue region is attributed to organic materials such as the ligand, oleylamine and the S/Se sources. The representative time-resolved photoluminescence (TRPL) of the nanocrystals at room temperature, measured with a weak 405 nm pulsed laser source, 435 nm long-pass filter, and collected through a spectrometer is shown in Fig. 1e. The photoluminescence lifetime of the green emission is 4 ns. Transient absorption measurements (350 nm pump, visible probe) of the same sample show a bleach feature from 500–650 nm, which provides another measure of the direct band gap (Fig. 1f). The transient absorption signal decays rapidly, showing a substantial reduction in absorbance within a few ps, which is an indication of ultrafast charge trapping. The charge carriers are expected to be electrons, as revealed by subsequent electronic structure calculations. The SEM, EDX,

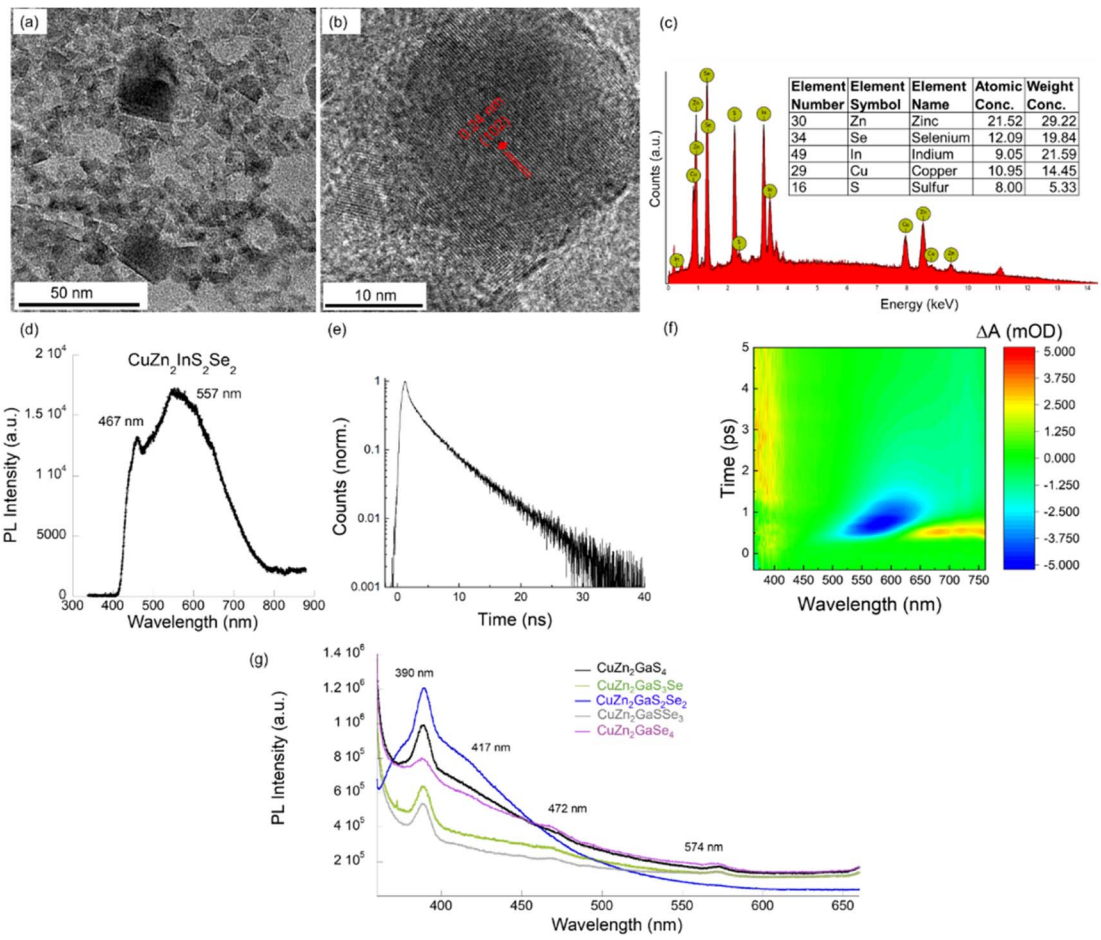

Fig. 1 Characterization of CZASSe nanocrystals. (a) TEM image, (b) HRTEM image, (c) SEM-EDX characterization, (d) PL spectrum, (e) TRPL plot, (f) transient absorption, all for $CuZn_2InS_2Se_2$ nanocrystals, and (g) PL spectra of various $CuZn_2GaS_xSe_{4-x}$ nanocrystal compositions. The results for other compositions are deposited in the ESI.†

and PL results for the other CZASSe compositions are shown in detail in the ESI (Fig. S1–S16†).

The composition-dependent change in the light-emitting properties of the CZASSe semiconductor nanocrystals has also been investigated. Fig. 1g shows the representative PL spectra of various compositions of the $CuZn_2GaS_xSe_{4-x}$ nanocrystals. Emissions in the violet region, *i.e.*, peak at 390 nm with a broad shoulder at 417 nm, blue (472 nm), and yellow (574 nm) regions of the visible spectrum are observed for all CZGaSSe compositions without significant peak shifts. However, the PL intensities at 390 nm and 417 nm decreased progressively with increased Se substitution with the exceptions of $CuZn_2GaS_2Se_2$ and $CuZn_2GaSe_4$. This can be attributed to the sizes of the respective nanocrystal compositions, *i.e.*, the smaller size of 7.66 nm for $CuZn_2GaS_2Se_2$ and the largest size of 13.17 nm for $CuZn_2GaSe_4$ (Table S1 and Fig. S17 ESI†). The PL intensity is the highest for the $CuZn_2GaS_2Se_2$ composition that can be attributed to the reduced size of the nanocrystals. The peak height at 390 nm (violet regime) decreased consistently with Se substitution with the exceptions of $CuZn_2GaS_2Se_2$ and $CuZn_2GaSe_4$, suggesting that the S chalcogen anion which decreased with Se substitution in the nanocrystal lattice may contribute to the emission at 390 nm.

The XRD structure of the CZASSe nanocrystals shows a pure wurtzite phase (space group: $P6_3mc$, no. 186).[32] The XRD plots for two representative CZASSe compositions, $CuZn_2GaS_3Se$ and $CuZn_2GaSe_4$, are shown in Fig. 2a and b, respectively. The major diffraction peaks at 2θ angles of 27.5°, 28.3°, 30.3°, 38.9°, 47°, 51.6°, 53.6°, 55.8°, and 59.4° for the $CuZn_2GaS_3Se$ nanocrystals can be indexed to (100), (002), (101), (102), (110), (103), (200), (112), and (201) crystal planes of the pure wurtzite phase. The average particle size of the nanocrystals is estimated using the Debye–Scherrer formula, which relates the size of the nanocrystallites in a solid to the broadening of a peak in the diffraction pattern:[33,34]

$$D = \frac{0.9\lambda}{\beta \cos \theta}$$

where λ is the wavelength of the X-ray radiation source Cu-Kα (1.5418 Å), β is the full width at half maximum (FWHM) corresponding to all the peaks on the diffraction pattern, θ is the diffraction angle for lattice planes, and D is the particle diameter size. By using all the diffraction peaks in the XRD pattern and taking the average of these peaks, the particle size of $CuZn_2GaS_3Se$ is calculated to be 9.87 nm (Table S1, ESI†). The diffraction peaks are shifted towards lower 2θ angles for the $CuZn_2GaSe_4$ composition, as expected, due to the larger size of the Se anion as compared to S. The average crystallite size of $CuZn_2GaSe_4$ is calculated to be 13.17 nm, based on the Debye–Scherrer equation and the XRD results (Table S1, ESI†). The XRD data of all the CZASSe semiconductor nanocrystals are shown in the ESI (Fig. S18–S20†). Additionally, the *d*-spacing, calculated from the 2θ angle of 37.7° for the (102) crystal plane for $CuZn_2InS_2Se_2$ nanocrystals is 2.38 Å, which matches the

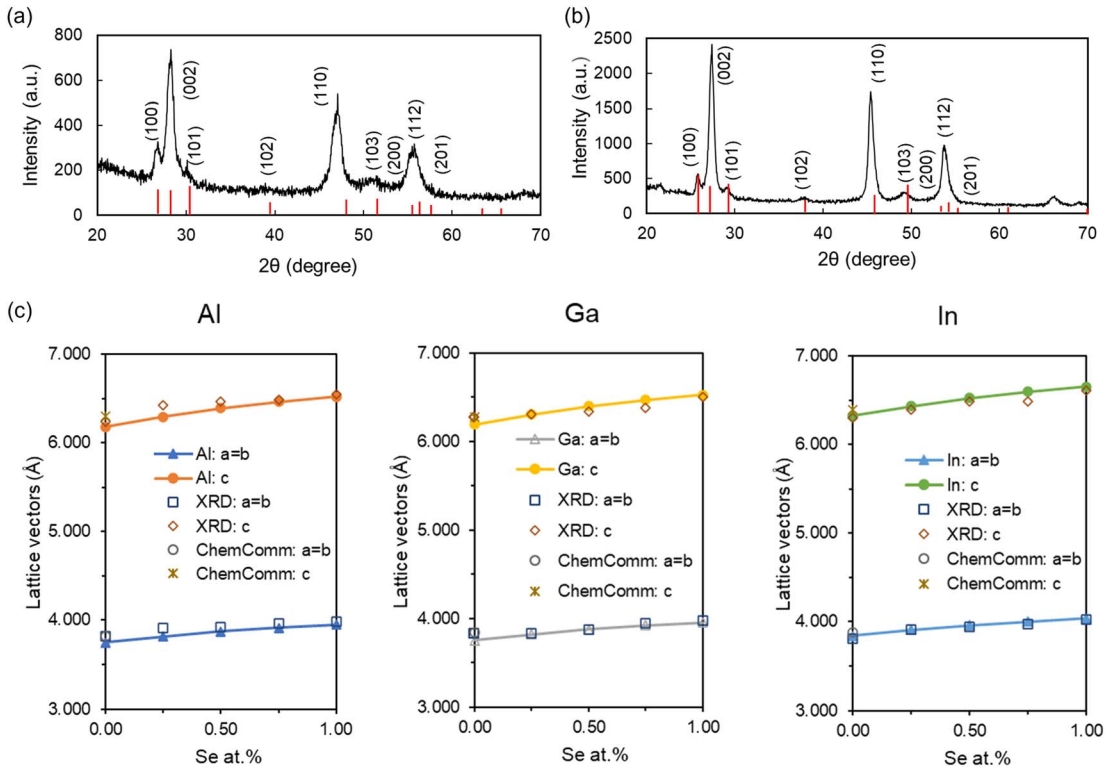

Fig. 2 XRD characterization of pure wurtzite phase CZASSe semiconductor nanocrystals. (a) XRD plots of $CuZn_2GaS_3Se$ nanocrystals and (b) XRD plot of $CuZn_2GaSe_4$ nanocrystals, where vertical lines represent peak positions obtained from theoretically relaxed crystal structures, and (c) plot showing a comparison of lattice parameters from theoretical three-dimensional structures, experimental XRD structures, and our previously reported CZAS nanocrystals in Chem. Commun.[13]

lattice spacing shown in the HRTEM image of the nanocrystal in Fig. 1b (Fig. S20, ESI†). The nanocrystals generally exhibit a wurtzite phase as suggested from the Rietveld refinement conducted using the GSA-II software (Fig. S21, ESI†). To lend further support to the experimental XRD results, we carried out DFT structural relaxation for the wurtzite phase structures using the SCAN meta-GGA functional, in conjunction with the VCA for S/Se alloying. The choice of this particular functional is based on recent studies showing that it works well for the compositionally related quaternary materials in the kesterite phase.[35] As can be seen from Fig. 2a and b, the peak positions obtained from the theoretically relaxed geometries agree approximately with the experimental diffraction peaks. The lattice parameters of different S : Se atomic compositions of $CuZn_2AlS_xSe_{4-x}$, $CuZn_2GaS_xSe_{4-x}$, and $CuZn_2InS_xSe_{4-x}$ nanocrystals show a close match between the values calculated based on the experimental XRD of pure wurtzite phase, the DFT calculated crystal structures of CZASSe compositions, as well as the lattice parameters of $CuZn_2AS_4$ that we reported earlier (Fig. 2c).

Both experimental and theoretical results indicate that the lattice parameters show an increasing trend with the progressive substitution of S atoms with the larger Se anion in the multinary chalcogenide compositions, as expected. The agreements of the diffraction peak positions and the lattice parameters validate the theoretically calculated crystal and atomic structures for all of the multinary chalcogenide compositions.

Using the theoretically relaxed geometries, we further calculated the electronic structures using both the SCAN meta-GGA and the HSE06 hybrid functionals for all of the multinary Cu-chalcogenide semiconductors synthesized in this work. Fig. 3a shows the unit cells of two representative $CuZn_2GaS_x$-Se_{4-x} compositions (*i.e.*, $CuZn_2GaS_4$ and $CuZn_2GaSe_4$) that have been used for the electronic structure calculations. The unit cells of the other CZGaSSe compositions are shown in Fig. S22 (ESI†). Fig. 3b shows the band structure and density of state

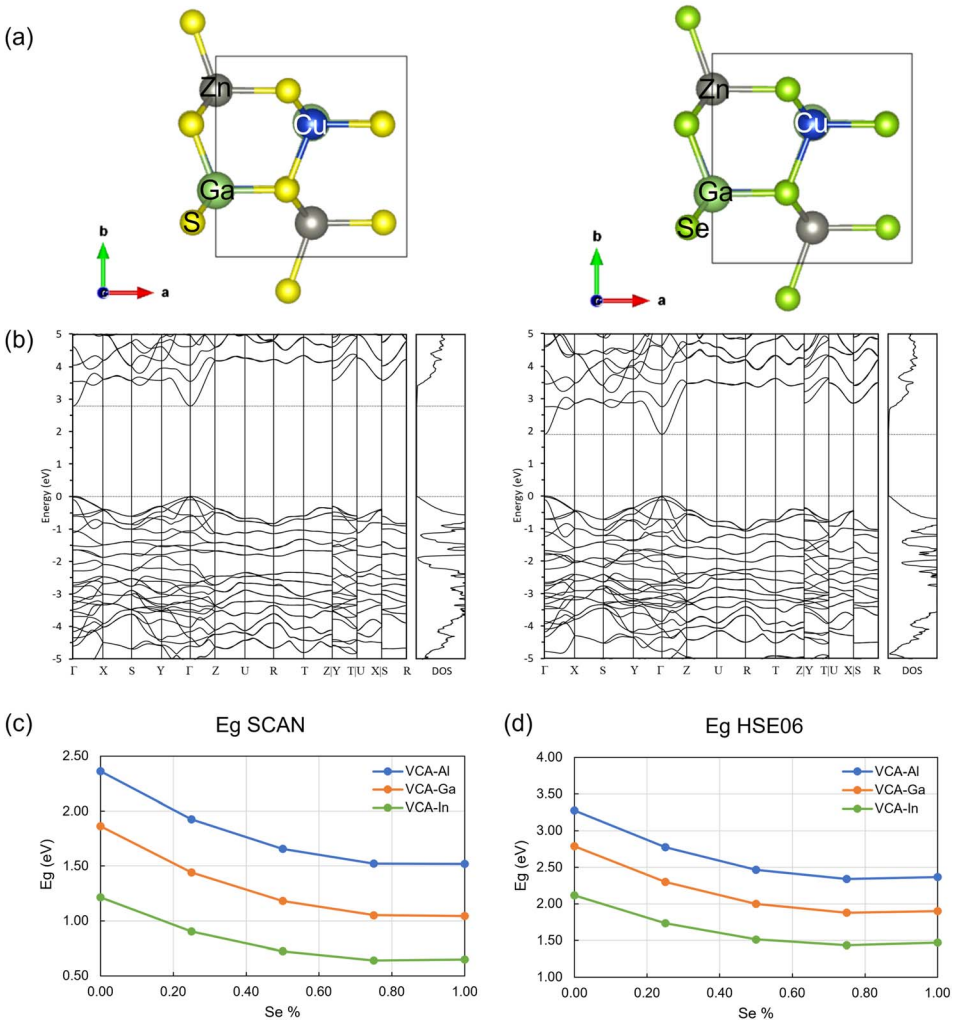

Fig. 3 Theoretical bandgap predictions of $CuZn_2AS_xSe_{4-x}$ nanocrystals *via* SCAN and HSE06 hybrid functionals along with virtual crystal approximation. (a) Unit cells of wurtzite phase $CuZn_2GaS_4$ (left) and $CuZn_2GaSe_4$ (right) used for electronic structure calculations, (b) plots showing HSE06 band structures and density of states of $CuZn_2GaS_4$ (left) and $CuZn_2GaSe_4$ (right), respectively. (c) SCAN and (d) HSE06 calculated direct bandgaps of CZAlSSe, CZGaSSe, and CZInSSe as a function of atomic% of Se.

(DOS) calculated with HSE06 functional for two representative compositions of $CuZn_2GaS_xSe_{4-x}$, one with S and other with Se. The electronic structures of the other S/Se and other CZASSe (A = Al and In) compositions are presented in the ESI (Fig. S23–S25†). All of these band structures display a direct bandgap at the Γ-point between valence and conduction bands with Dirac band characteristics.[36] It is also worth noting that the conduction band is more dispersive than the valence bands; therefore, the mobility of electrons is expected to be higher than that of holes, making the former the dominant charge carriers, which are observed in the transient absorption signals (Fig. 1f). The bands with S and Se as the anions are similar but the bandgap is reduced upon replacement of S with Se. The bandgaps calculated by both SCAN meta-GGA and HSE06 hybrid functionals of the multinary CZASSe compositions decrease with increased size of the group III cation *i.e.*, Al > Ga > In (Fig. 3c, d and S23–S25, ESI†). In addition, the bandgaps of the S/Se alloying compositions also show a clear trend of decrease with increased substitution of S with Se anions in the multinary unit cell until x = 0.75–1.00, where the bandgap becomes comparable (Fig. 3c and d). These trends align with observations in other materials where both chemical doping or mechanical stretching have been demonstrated to induce lattice expansions (as shown in Fig. 2c, 3c and d), consequently leading to reduced orbital overlaps and narrower spacings between bands.[37] Between the results calculated with the two different functionals, the HSE06 bandgaps are significantly enhanced from the SCAN results. Nevertheless, they show the same trends with the compositional changes, in particular induced by the S/Se alloying, which significantly broadens and diversifies the electronic and optical absorption properties of CZASSe nanocrystals. It is worth pointing out that the HSE06 exchange–correlation functional, which is known for accuracy in bandgap predictions, produces bandgaps that fall in the visible range of *ca.* 1.5–3.2 eV, which are relevant for practical applications such as photovoltaics, photocatalysts, sensors, and light emitting diodes.

The corresponding experimental optical properties of the CZASSe semiconductor nanocrystals are investigated *via* UV-vis spectroscopy of the well dispersed colloidal solutions of the nanocrystals in hexane. Fig. 4a shows the UV-vis spectrum of a representative CZASSe composition, $CuZn_2AlS_2Se_2$ nanocrystals. The direct optical bandgap (E_g) of the semiconductor nanocrystals is determined by extrapolating the linear region of the Tauc *i.e.*, $(A\hbar\nu)^2$ *versus* $\hbar\nu$ plot, where A is the absorbance, $\hbar$ is Planck's constant, and ν is the frequency of absorbed light. $CuZn_2AlS_2Se_2$ nanocrystals exhibit a direct bandgap of 2.41 eV in the visible cyan regime of the visible solar spectrum, making it highly attractive for photovoltaic applications (Fig. 4b). Detailed experimental direct bandgap of each of the CZASSe nanocrystals is shown in the ESI (Fig. S26–S28†) and summarized in Table S1, ESI.† In general, the bandgap trend agrees with the theoretical *ab initio* predictions. However, the theoretical bandgaps have been calculated for bulk materials to reveal the general trends to be used as a reference, while experimental factors such as the size of nanocrystals, morphology, and defects can also play a role in the experimental bandgap of the semiconductor nanocrystals in addition to the S : Se composition.[38–40] Therefore, the deviations from theory can be attributed to the variations of size, morphology, and defects in the CZASSe nanocrystals.

In this work, a novel class of multinary Cu-chalcogenide nanocrystals, $CuZn_2AS_xSe_{4-x}$ has been synthesized for the first time as new and more sustainable semiconductor materials with diversified electronic and optical properties for light absorbing and light-emitting applications. The new chalcogenide nanocrystals exhibit a wurtzite phase, as seen from the XRD structures and Rietveld refinement. The size and morphology of the nanocrystals have been characterized *via* TEM and SEM and show a highly crystalline wurtzite phase structure. The multinary semiconductor nanocrystals exhibit composition-dependent tunable direct bandgap and photoluminescence in the visible range, as suggested by the experimental UV-vis, Tauc, and PL plots. We also report the TRPL characterization of the new nanocrystals. Additionally, three-

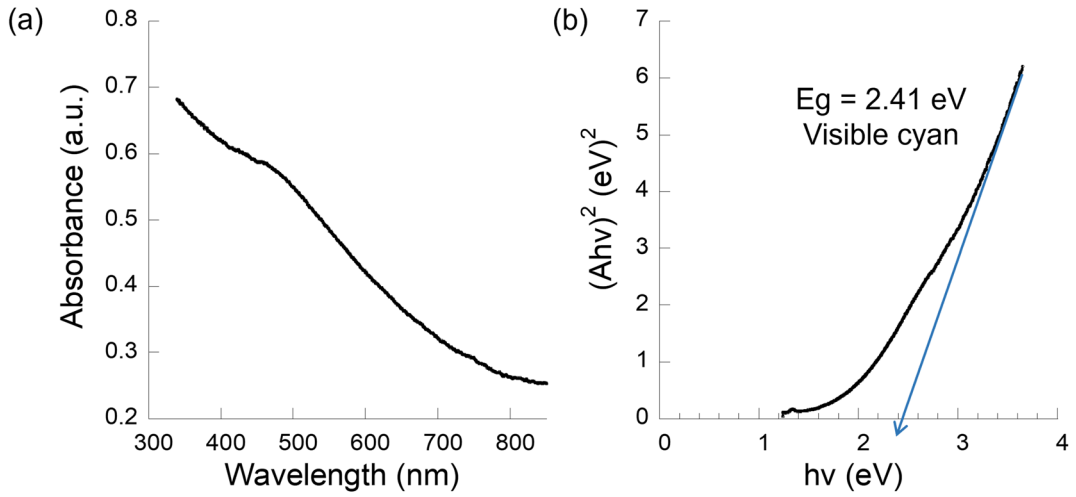

Fig. 4 Experimental bandgap measurements of pure wurtzite phase $CuZn_2AlS_2Se_2$ nanocrystals. (a) UV-vis plot and (b) Tauc plot showing direct bandgap.

dimensional unit cells of the various multinary compositions have been modeled using DFT calculations employing the SCAN meta-GGA and HSE06 hybrid functionals, in conjunction with VCA approximation, which show close match with the experimental lattice parameters and diffractions from our XRD structures. A decrease in bandgap with increased size of the group III cation and increased substitution of S with the larger Se anion is predicted from the theoretical measurements. Size, morphology, and defect may also affect the physical properties of the multinary nanocrystals. For example, Fig. S17 (ESI†) shows the trend of experimental bandgap of the CZASSe nanocrystals. A comparison of the experimentally derived bandgap with that obtained using the two theoretical methods is shown in Table S1 (ESI†). In general, the HSE06 shows a closer match with experimentally derived bandgap. The calculations for $CuZn_2AS_4$ and $CuZn_2AS_3Se$ compositions agree closely with experiment and larger deviations from experiment are observed with increased substitution of Se in the nanocrystal compositions. The deviation from experiment also increases with increased size of the group III cation in the CZASSe compositions (Table S1, ESI†). The experimental results display a general trend of decreasing bandgap with increasing amount of Se, which is confirmed by calculations. However, the effects of group III elements is not clear, which should be ascribed to other factors including particle sizes. In comparison, theoretical calculations also show the trend for group III elements. The bandgaps calculated with hybrid functional all fall in the visible range rendering them relevant for practical applications.

Author contributions

SP conceptualized the experiments, conducted the experiments, analyzed the results, and wrote the manuscript, SS conducted the syntheses and SEM characterization, JC contributed to the synthesis and manuscript revision, BD conducted the advanced TEM and PL analyses and wrote the manuscript, PG contributed to discussion and analysis of results and manuscript revision, and JH conceptualized the theory, conducted the theoretical calculations, analyzed the results, and wrote the manuscript.

Conflicts of interest

There are no conflicts to declare.

Acknowledgements

This work was supported by the Intel Ohio-southwest Alliance on Semiconductors and Integrated Scalable Manufacturing (OASIS) grant, and National Science Foundation REU Award #2244146, CNM ANL user project, and CNMS ORNL user project. TEM and TRPL were performed at the Center for Nanoscale Materials (CNM), a US Department of Energy Office of Science User Facility at Argonne National Laboratory, supported by the Office of Basic Energy Sciences under contract no. DE-AC02-06CH11357. DFT calculations were conducted at the Center for Nanophase Materials Sciences (CNMS), which is a US Department of Energy Office of Science User Facility at Oak Ridge National Laboratory.

Notes and references

1 L.-X. Yang, S. Zhang, B. Xu, J. Jiang, B. Cai, X. Lv, Y. Zou, Z. Fan, H. Yang and H. Zeng, *Nano Lett.*, 2023, **23**, 2443.
2 T. Todorov, O. Gunawan, S. Chey, T.-G. de Monsabert, A. Prabhakar and D.-B. Mitzi, *Thin Solid Films*, 2011, **519**, 7378.
3 U. Ghorpade, M. Suryawanshi, S. Shin, K. Gurav, P. Patil, S. Pawar, C. Hong, J. Kim and S. Kolekar, *Chem. Commun.*, 2014, **50**, 11258.
4 M.-A. Green, K. Emery, Y. Hishikawa, W. Warta and E.-D. Dunlop, *Prog. Photovoltaics*, 2016, **24**, 3.
5 J. Zhou, X. Su, Q. Huang, B. Zhang, J. Yang, Y. Zhao and G. Hou, *J. Mater. Chem. A*, 2022, **10**, 20147.
6 S. Hadke, M.-L. Huang, C. Chen, Y. Tay, S. Chen, J. Tang and L. Wong, *Chem. Rev.*, 2022, **122**, 10170.
7 A. Kumar, A. K. Goyal, U. Gupta, Tanya, N. Gupta and R. Chaujar, *Mater. Today: Proc.*, 2020, **28**, 361.
8 T.-S. Lopes, J.-P. Teixeira, M.-A. Curado, B.-R. Ferreira, A.-J.-N. Oliveira, J.-M. Cunha, M. Monteiro, A. Violas, J.-R.-S. Barbosa, P.-C. Sousa, *et al.*, *npj Flexible Electron.*, 2023, **7**, 4.
9 R.-B. Wexler, G.-S. Gautam and E.-A. Carter, *J. Mater. Chem. A*, 2021, **9**, 9882.
10 D.-B. Mitzi and Y. Kim, *Faraday Discuss.*, 2022, **239**, 9–37.
11 J. Li, J. Huang, F. Ma, H. Sun, J. Cong, K. Privat, R.-F. Webster, S. Cheong, Y. Yao, R.-L. Chin, *et al.*, *Nat. Energy*, 2022, **7**, 754.
12 W. Wang, M.-T. Winkler, O. Gunawan, T. Gokmen, T.-K. Todorov, Y. Zhu and D.-B. Mitzi, *Adv. Energy Mater.*, 2014, **4**, 1301465.
13 A. Ghosh, S. Palchoudhury, T. Rajalingam, Z. Zhou, N. Naghibolashrafi, K. Ramasamy and A. Gupta, *Chem. Commun.*, 2016, **52**, 264.
14 S. Palchoudhury, K. Ramasamy and A. Gupta, *Nanoscale Adv.*, 2020, **2**, 3069.
15 S. Palchoudhury, K. Ramasamy, J. Han, P. Chen and A. Gupta, *Nanoscale Adv.*, 2023, **5**, 2724.
16 F. Wang, Y. Han, C. Lim, Y. Lu, J. Wang, J. Xu, H. Chen, C. Zhang, M. Hong and X. Liu, *Nature*, 2010, **463**, 1061.
17 Y. Li, Z. Li, X. Wang, F. Liu, Y. Cheng, B. Zhang and D.-L. Shi, *Theranostics*, 2012, **2**, 769.
18 Quantum Leaps, *Nat. Biotechnol.*, 2006, **24**, 305.
19 A. Kamath, C. Melnychuk and P. Guyot-Sionnest, *J. Am. Chem. Soc.*, 2021, **143**, 19567.
20 S.-E. Keuleyan, P. Guyot-Sionnest, C. Delerue and G. Allan, *ACS Nano*, 2014, **8**, 8676.
21 X. Liang, E.-G. Durmusoglu, M. Lunina, P.-L. Hernandez-Martinez, V. Valuckas, F. Yan, Y. Lekina, V.-K. Sharma, T. Yin, S.-T. Ha, *et al.*, *ACS Nano*, 2023, **17**, 19981.
22 J.-Z. Kubicek-Sutherland, N.-S. Makarov, Z.-R. Stromberg, K.-D. Lenz, C. Castañeda, A.-N. Mercer, H. Mukundan, H. McDaniel and K. Ramasamy, *ACS Appl. Bio Mater.*, 2020, **3**, 8567.
23 Y.-T. Zhong, Z.-R. Ma, S.-J. Zhu, J.-Y. Yue, M.-X. Zhang, A.-L. Antaris, J. Yuan, R. Cui, H. Wan, Y. Zhou, W.-Z. Wang, *et al.*, *Nat. Commun.*, 2017, **8**, 737.

24 J. Sun, A. Ruzsinszky and J.-P. Perdew, *Phys. Rev. Lett.*, 2015, **115**, 036402.
25 J. Heyd, J.-E. Peralta, G.-E. Scuseria and R.-L. Martin, *J. Chem. Phys.*, 2005, **123**, 174101.
26 L. Bellaiche and D. Vanderbilt, *Phys. Rev. B: Condens. Matter Mater. Phys.*, 2000, **61**, 7877.
27 G. Kresse, *J. Non-Cryst. Solids*, 1995, **193**, 222.
28 G. Kresse and J. Furthmuller, *Phys. Rev. B: Condens. Matter Mater. Phys.*, 1996, **54**, 11169.
29 P.-E. Blochl, *Phys. Rev. B: Condens. Matter Mater. Phys.*, 1994, **50**, 17953.
30 G. Kresse and D. Joubert, *Phys. Rev. B: Condens. Matter Mater. Phys.*, 1999, **59**, 1758.
31 W. Setyawan and S. Curtarolo, *Comput. Mater. Sci.*, 2010, **49**, 299.
32 X. Shen, E.-A. Hernandez-Pagan, W. Zhou, Y.-S. Puzyrev, J.-C. Idrobo, J.-E. Macdonald, S.-J. Pennycook and S.-T. Pantelides, *Nat. Commun.*, 2014, **5**, 5431.
33 A. O. Bokuniaeva and A. S. Vorokh, *J. Phys.: Conf. Ser.*, 2019, **1410**, 012057.
34 J.-M. Wu and Y.-R. Chen, *J. Phys. Chem. C*, 2011, **115**, 2235.
35 T. Ratz, J.-Y. Raty, G. Brammertz, B. Vermang and N.-D. Nguyen, *J. Phys.: Energy*, 2021, **3**, 035005.
36 C. Hu, X. Zeng, Y. Liu, M. Zhou, H. Zhao, T. Tritt, J. He, J. Jakowski, P.-R.-C. Kent, J. Huang, *et al.*, *Phys. Rev. B*, 2017, **95**, 165204.
37 A. Chaves, J.-G. Azadani, H. Alsalman, D.-R. da Costa, R. Frisenda, A.-J. Chaves, S. Song, Y. Kim, D. He, J. Zhou, *et al.*, *npj 2D Mater. Appl.*, 2020, **4**, 29.
38 L. Brus, *J. Phys. Chem.*, 1986, **90**, 2555.
39 A.-M. Smith and S. Nie, *Acc. Chem. Res.*, 2010, **43**, 190.
40 T. Kippeny, L.-A. Swafford and S.-J. Rosenthal, *J. Chem. Educ.*, 2002, **79**, 1094.